International Journal of Thermophysics, Vol. 26, No. 4, July 2005 (© 2005)
DOI: 10.1007/s10765-005-6685-9

Numerical Simulation of Fast Dynamic Laser-Surface Interaction during Laser-Induced Modification Processes of Ceramic Substrates[1]

M. Rohde,[2,3] O. Baldus,[2] D. Dimitrova,[2] and S. Schreck[2]

Laser-supported processes can be used to modify the electrical and thermal properties of ceramic substrates locally. These processes are characterized by a strong thermal interaction between the laser beam and the ceramic surface which leads to localized melting. During the dynamic melting process, an additive material is injected into the melt pool in order to modify the physical properties. The heat and mass transfer during this dynamic melting and solidification process has been studied numerically in order to identify the dominating process parameters. Simulation tools based on a finite volume method have been developed to describe the heat transfer, fluid flow, and the phase change during the melting and solidification of the ceramic. The results of the calculations have been validated against experimental results.

KEY WORDS: laser; melting; phase change; surface modification.

1. INTRODUCTION

Laser-supported surface dispersing and alloying of ceramics are important methods to modify the properties of this class of brittle and nonconducting materials. Using this laser process, mechanical and tribological properties [1] can be improved, and thermal and electrical conductances can be adjusted [2, 3]. Furthermore, the property modifications are restricted to a localized area leaving the bulk of the ceramic in its original state. However, due to the complex relationship between the process parameters and

---

[1] Paper presented at the Seventh International Workshop on Subsecond Thermophysics, October 6–8, 2004, Orléans, France.

[2] Forschungszentrum Karlsruhe GmbH, Institut für Materialforschung I, Hermann-von-Helmholtz-Platz 1, 76344 Eggenstein-Leopoldshafen, Germany.

[3] To whom correspondence should be addressed. E-mail: magnus.rohde@imf.fzk.de

results of the laser alloying, optimization procedures are often time consuming and only guided by a long-term experimental experience. Therefore, simulation tools with the ability to predict experimental results, or at least to restrict parameter fields, would be helpful to reduce the time of the process development.

In this paper we study the dynamic liquid–solid phase change and the distribution of the second phase within the melt pool generated during the process as a function of the process parameters. The temperature and velocity profiles have been calculated for both phases, i.e., the molten alumina and the dispersed metal phase, by the CFD-code PHOENICS [4], which uses the finite volume method to integrate the corresponding energy and Navier-Stokes equations, respectively. For the modeling of the liquid-solid phase change process, an enthalpy-porosity technique is applied. In particular, the laser-induced dispersing of TiN particles into Al_2O_3 substrates has been considered in this study within a comparison of two different process modes.

2. LASER PROCESS

The principle of the process is shown in Fig. 1. The laser beam of a high-power CO_2-laser is used to heat the surface of the ceramic above the melting point. Metallic particles are introduced into the localized melt pool. After the solidification, a metal-ceramic composite has been generated within the laser-irradiated trace. This can be achieved by using a one- or two-step process (see Fig. 1). In the one-step process the particles are introduced by injection during the laser-solid interaction while the two-step process uses a pre-placed powder coating which is applied to the ceramic surface prior to the laser-induced melting. During the laser

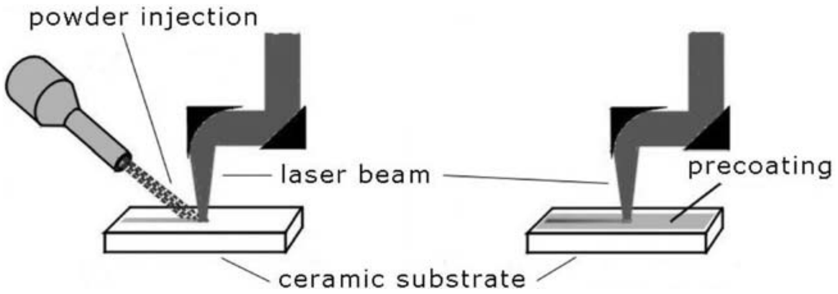

Fig. 1. Schematics of the laser-induced surface modification. One-step process (left): particles are injected into the melt pool through a nozzle during the laser process. Two-step process (right): a coating of metallic particles is applied prior to the laser process.

process the ceramic substrate is heated to avoid thermally induced cracking. In order to generate modified lines or regions, the substrate is moved relative to the laser position with a constant velocity. For most experiments a CO_2-laser ($\lambda_{CO2} = 10.6\mu m$) with a maximum power of 500 W was used. The laser beam was shaped by line optics giving a rectangular intensity distribution with a length of 1 mm and width of 6 mm. The laser power was varied between 200 and 400 W. The travelling velocity of the laser beam or the substrate was typically adjusted between 125 and $500\,\mathrm{mm} \cdot \mathrm{min}^{-1}$.

3. NUMERICAL METHOD

The CFD-software PHOENICS [4] has been used to solve the Navier-Stokes equations which describe the fluid flow within the melt pool due to the surface-tension gradient (Marangoni convection) that is induced by the localized heat source travelling with a constant speed. The heat source is generated by a focused laser beam with a strip-like intensity profile which superimposes a strong transient temperature gradient on the surface. Temperature-dependent material properties such as the thermal conductivity and heat capacity have been included in the model. The computation has been performed under the assumptions that the flow is laminar, the fluid is incompressible with a flat-free surface, and the Boussinesq approximation is valid for the density variation within the melt.

The governing equations, which describe the velocity and temperature distribution, for the numerical modeling of the process are

$$\text{continuity} \quad \frac{\partial(\rho u)}{\partial x} + \frac{\partial(\rho v)}{\partial y} = 0 \tag{1}$$

$$x\text{-momentum} \quad \frac{\partial u}{\partial t} + u \cdot \nabla u = -\frac{1}{\rho}\frac{\partial P}{\partial x} + \mu\,\Delta u \tag{2}$$

$$y\text{-momentum} \quad \frac{\partial v}{\partial t} + v \cdot \nabla v = -\frac{1}{\rho}\frac{\partial P}{\partial x} + \mu \Delta v - \beta g \cdot (T - T_M) \tag{3}$$

$$\text{energy} \quad \frac{\partial T}{\partial t} + u \cdot \frac{\partial T}{\partial x} + v \cdot \frac{\partial T}{\partial y} = \kappa \cdot \Delta T \tag{4}$$

with the boundary conditions at the surface at $y = 0$

$$v = 0 \tag{5}$$

$$\mu \cdot \frac{\partial v}{\partial y} = -\frac{\partial \sigma}{\partial T}\frac{\partial T}{\partial x} \tag{6}$$

$$Q_{\mathrm{Las}} = P_{\mathrm{Las}}\,(v_{\mathrm{Scan}}, t) \cdot \left(\frac{1}{1+e^{-(x-x_0)/f}} + \frac{1}{1+e^{(x-x_0)/f}} \right) + 1 \tag{7}$$

where u and v are the x- and y-velocity components, respectively, t, x, y are the time and space coordinates in the 2D-model, T is the temperature, P is the pressure, ρ is the density of the material, μ is the viscosity, κ is the thermal diffusivity, g is the gravitational constant, and T_M is the melting temperature. The boundary conditions given by Eqs. (5)–(7) account for the fact that the y-component of the velocity field vanishes (Eq. (5)) at the free surface, that shear forces are generated (Eq. (6)) at the surface of the melt pool due to a gradient in the surface tension σ, and that a time-dependent heat flux Q_{Las} through the liquid-gas boundary (Eq. (7)) is induced due to the absorption of the laser energy with a rectangular ($6\times1\,\mathrm{mm}^2$) intensity profile. The first term P_{Las} in Eq. (7) accounts for the time-dependent part of the heating profile, which is determined by the scanning velocity v_{Scan} of the laser beam. The second term describes the lateral variation of the profile.

The transport of the alloying material due to convection and diffusion within the melt pool can be expressed by

$$\frac{\partial(\rho C)}{\partial t} + \frac{\partial(\rho u C)}{\partial x} + \frac{\partial(\rho v C)}{\partial y} = \frac{\partial}{\partial x}\left(D\frac{\partial C}{\partial x}\right) + \frac{\partial}{\partial y}\left(D\frac{\partial C}{\partial y}\right) \tag{8}$$

where D is the diffusion coefficient and C is the mass fraction.

The moving melting-solidification boundary and the liquid-solid phase change have been considered in the model by implementing the enthalpy-porosity method [5, 6] into PHOENICS. In order to achieve this implementation, additional source terms have been introduced in the momentum, Eqs. (2) and (3), and energy equations, Eq. (4), which take into account that the velocity components vanish in the solid phase and that the enthalpy changes due to the latent heat during the melting process. The PHOENICS user interface "In-Form", which allows for the transmission of mathematical expressions to the solver by input of formulas in the model description files, has been used to implement these terms.

The enthalpy and porosity functions, $F(T)$ and $A(T)$, which were introduced for the simulations within this study, are given in the following two equations, respectively.

$$F(T) = \frac{1}{1+e^{-(T-T_M)/\varepsilon}} \tag{9}$$

$$A(T) = \frac{C(1-F)^2}{F^3+q};\ q = 0.001;\ C = 1.5\cdot10^3 \tag{10}$$

The values of constants C and q are chosen as results of test simulations. The functions given by Eqs. (9) and (10) have been introduced into the momentum and energy equations as additional source terms:

$$\frac{\partial \upsilon}{\partial t} + \upsilon \cdot \nabla \upsilon = -\frac{1}{\rho}\frac{\partial P}{\partial x} + \mu \Delta \upsilon - A \cdot (\upsilon - \upsilon_{\mathrm{Scan}}) \qquad (11)$$

$$\frac{\partial \nu}{\partial t} + \nu \cdot \nabla \nu = -\frac{1}{\rho}\frac{\partial P}{\partial y} + \mu \Delta \nu - \rho\beta g \cdot (T - T_M) - A \cdot (\nu - \nu_{\mathrm{Scan}}) \qquad (12)$$

$$\frac{\partial T}{\partial t} + \upsilon \cdot \frac{\partial T}{\partial x} + \nu \cdot \frac{\partial T}{\partial y} = \kappa \cdot \Delta T - L \cdot \left[\frac{\partial(\rho F)}{\partial t} + \frac{\partial(\rho \upsilon F)}{\partial x} + \frac{\partial(\rho \nu F)}{\partial y}\right] \qquad (13)$$

At temperatures above the melting temperature T_M, the porosity function A vanishes and F, which can be taken as a fraction of the liquid phase, equals one. Therefore, the additional source terms also reduce to zero, which leads to the normal form of the Navier-Stokes equations given by Eqs. (2)–(4), since the continuity equations are not affected. At temperatures below T_M, A increases to high values and consequently reduces the velocity components close to nearly zero. Since the liquid fraction is also zero, the system of equations reduces to an expression for heat diffusion within a solid, since the convection terms are suppressed. The second term of the RHS of Eq. (13), which takes the evolution of the latent heat L at the melting or solidification front into account, contributes nonzero values only close to the melting point.

For the calculations the surface tension coefficient of molten Al_2O_3, $d\sigma/dT = -6\times\ 10^{-5}\ \mathrm{kg\cdot s^{-2\cdot\circ}C^{-1}}$, and the viscosity of $\mu = 0.105\,\mathrm{kg\cdot m^{-1}\cdot s^{-1}}$ [7–9] have been used in the boundary condition, Eq. (6). The other relevant thermophysical parameters for alumina like the thermal conductivity and the heat capacity have been measured using standard methods [3] up to a temperature of 1400°C and extrapolated to the melting temperature. This gives a value of $4.5\,\mathrm{W\cdot m^{-1}\cdot K^{-1}}$ for the thermal conductivity and $1500\,\mathrm{J\cdot kg^{-1}\cdot K^{-1}}$ for the specific heat at the melting point which are in agreement with the measured data by Paradis et al. [10]. In the case of TiN, the data have been taken from the literature [11].

4. RESULTS AND DISCUSSION

The model geometry and the numerical results calculated by the two-dimensional FV-model for the case of the laser-induced dispersing of

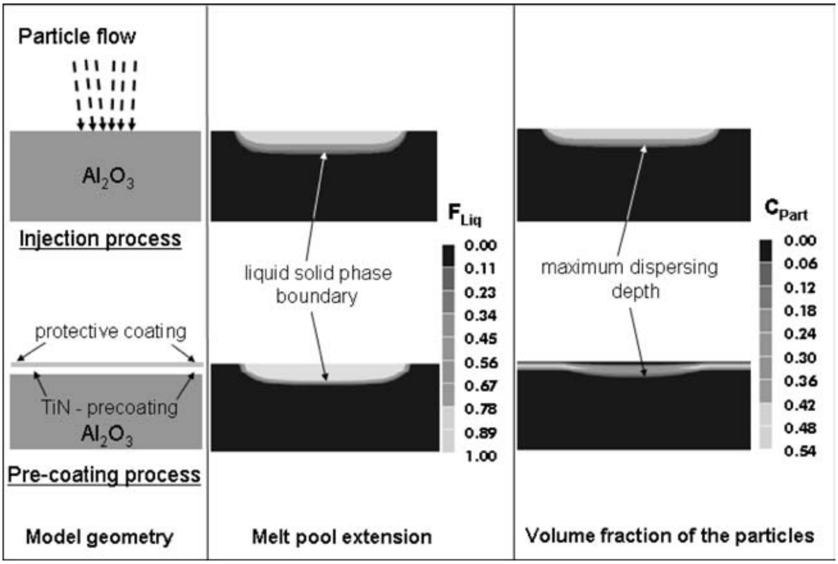

Fig. 2. Model geometry used in the FV-simulation, calculated results for the extension of the melt pool and distribution of the TiN phase (R2); (top) one-step injection process, (bottom) two-step pre-coating process.

TiN into Al_2O_3 are shown in Fig. 2 for the one-step and two-step processes, respectively. The extension of the melting pool, and also the distribution of the additive material, exhibit different characteristics, depending on the process option used. In the case of the one-step process, the shear forces at the surface of the alumina substrate induced by the finite temperature coefficient of the surface tension lead to a flat but wide melting pool. The second phase (TiN) is distributed homogeneously only down to a certain dispersing depth which is lower than the maximum depth of the melting pool. In the two-step process with the pre-coating and the protective overlayer, the absence of shear forces leads to a slow sedimentation of the second phase into the molten region of the substrate. During the laser-induced re-melting of the substrate and the overlayer, the TiN pre-coating is infiltrated by molten alumina at early stages of the process and starts to sink into the molten pool later. After solidification, the main part of the metal-ceramic composite has been developed as a layer on top of the surface of the substrate in contrast to the one-step process, where the second phase is incorporated completely.

In order to get more insight in the dominating process parameters, further simulations have been performed with variations of the laser power and the scanning speed in order to obtain a parameter field

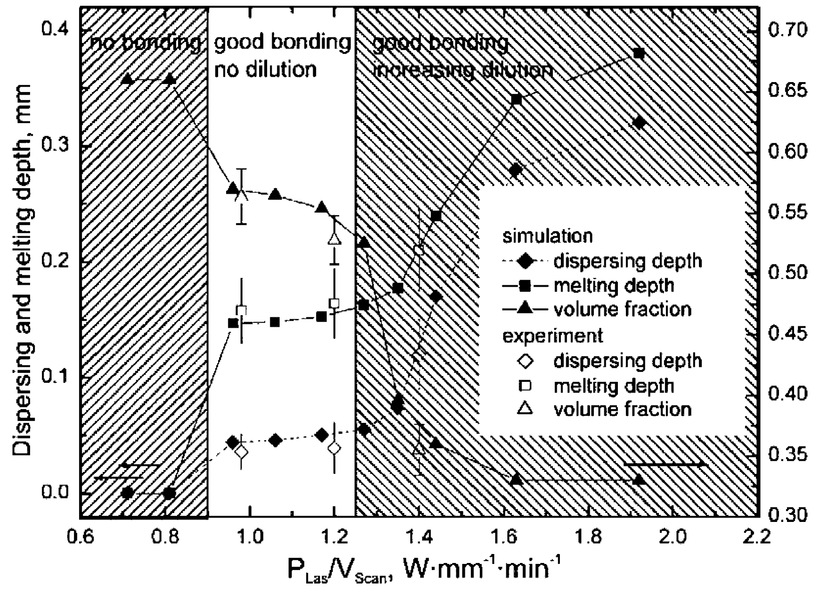

Fig. 3. Calculated depths of dispersing and melting and maximum volume fraction of TiN in Al_2O_3 as a function of the laser power divided by the scanning speed P_{Las}/V_{Las}.

which is also relevant for the experimental process development. Calculated melting and dispersing depths and the maximum volume fraction of the dispersed TiN phase as a function of the laser power divided by the laser scanning speed P_{Las}/V_{Scan} are shown in Fig. 3 for processing with a preplaced TiN-coating. This value gives a measure of the effective heating along the laser scanning line which is high for low scanning speeds and high laser power and tends to be small with increasing scanning speed due to the fact that the laser-surface interaction time decreases. For the simulations thickness values of 200 μm for TiN precoating and 100 μm for the Al_2O_3 overlayer have been used. Scanning velocities of 125, 250, and 500 mm · min^{-1} have been used within the model, and the laser power has been varied between 200 and 480 W. From the diagram critical effective heating levels can be extracted where the characteristic behavior of the melting/dispersing depths and also the TiN-volume fraction changes as a function of the laser-process parameter. Three different regions can be identified. For P_{Las}/V_{Scan}-values less than 0.9 W · mm^{-1} · min^{-1}, the preplaced TiN-powder has no coupling to the ceramic substrate since the TiN-volume fraction is relatively high but the melting and dispersing depths are zero. Within this region the effective heating energy is too small to raise the surface temperature of the ceramic above the melting point. In the second regime ranging from 0.9 to $1.25\,\mathrm{W \cdot mm^{-1} \cdot min^{-1}}$, a metal-ceramic composite is generated on top of the surface. The melting and dispersing depths vary only slightly on a low level within this parameter range, but the TiN-volume fraction stays relatively high. At higher effective heating levels above $1.25\,\mathrm{W \cdot mm^{-1} \cdot min^{-1}}$, the TiN pre-coating starts to sink into the growing melt pool which consequently leads to a larger dispersing depth but also to an increased dilution of TiN particles as reflected by the decrease in the volume fraction. The results of the simulation have been confirmed by experimental data. This specific behavior of the second-phase pre-coating during the laser-induced surface modification is also illustrated in the cross-sectional micrographs shown in Fig. 4.

The results of the simulation of the one-step injection process are shown in Fig. 5. The model calculations have been performed with varying laser powers between 200 and 300 W. The scanning speed of the laser has been adjusted to the values 125, 250, and $500\,\mathrm{mm \cdot s^{-1}}$. The mass flux of the TiN particles was $270\,\mathrm{mg \cdot cm^{-2} \cdot s^{-1}}$. The overall level of the power density is significantly less than for the two-step process since there is no pre-coating layer which can act as a thermal barrier.

The dispersing and melting depths vary smoothly as a function of the laser power divided by the scanning speed $P_{\mathrm{Las}}/V_{\mathrm{scan}}$ with this process option. The volume fraction increases also with higher laser power but reaches a saturation value of approximately 60% at the highest level. A critical level on the P/V scale, which separates a region where a composite layer on top of the surface develops, from a regime that is characterized by the settling of the metal particles below the original surface of the substrate, cannot be observed as in the case of the pre-coating process.

5. SUMMARY AND CONCLUSION

A numerical model has been presented for the simulation of laser-induced surface modification processes of ceramics. Two process options have been considered in the model for the transfer of a second phase material into the ceramic substrate: a pre-coating process which utilizes a metallic layer applied prior to the laser-solid interaction and an injection process in which a powder flow is directed onto the ceramic surface during the laser-induced re-melting. For the injection process the mass transport within the molten ceramic pool is driven by the temperature coefficient of the surface tension at the liquid-gas interface. In the pre-coating process the slow sedimentation of the second phase leads to a

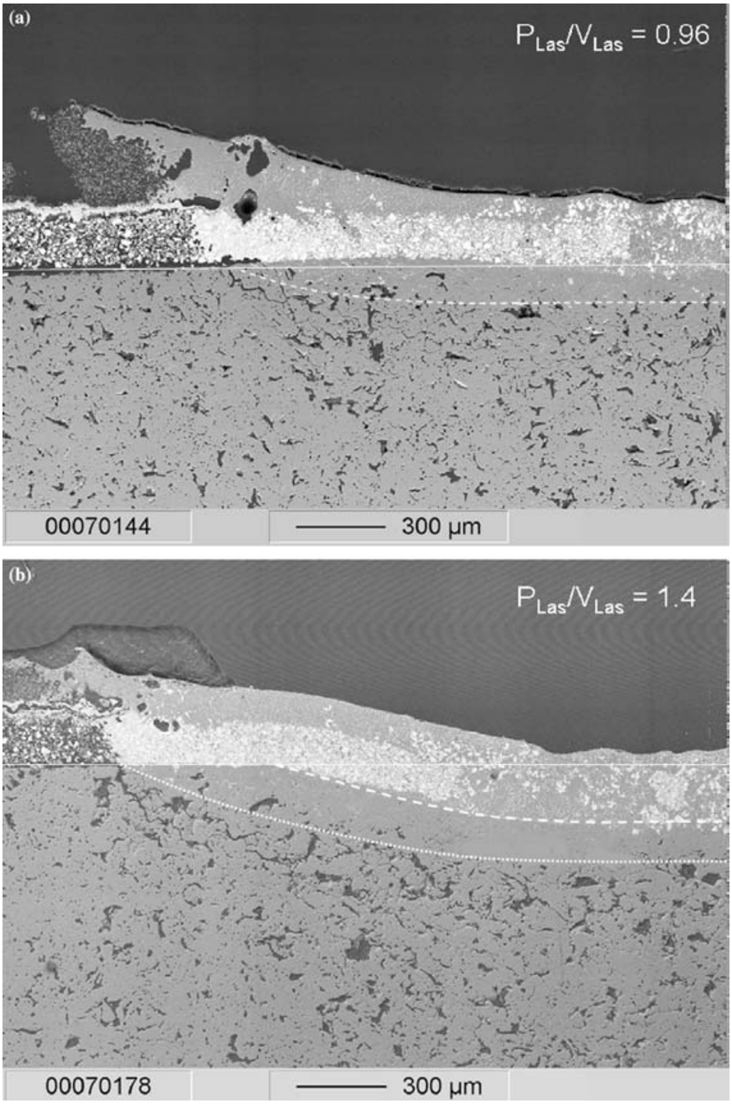

Fig. 4. Cross section of the laser-modified region of the Al_2O_3-substrate at different values of the laser power divided by the scanning speed P_{Las}/V_{Las}. White line marks the original surface of the substrate: (a) Average dispersing depth is only slightly below the original surface level for this particular P_{Las}/V_{Las}-value. Melting depth is marked by the dashed line. (b) Dispersing depth—marked by the dashed line—is below the original surface at higher values of P_{Las}/V_{Las}. Melting depth is marked by dotted white line.

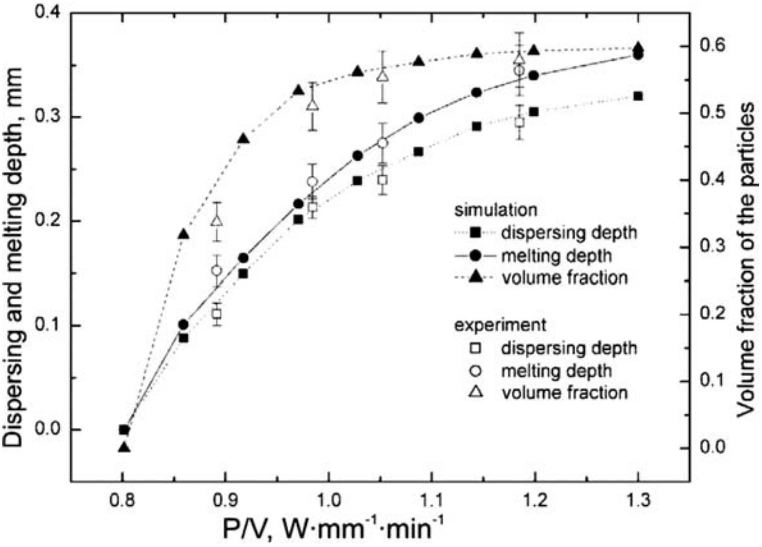

Fig. 5. Calculated dispersing and melting depths and volume fraction of the TiN phase for the injection process as a function of the power density divided by the scanning speed of the laser.

distribution of metal particles which shows characteristic features depending on the laser power density in a critical way.

ACKNOWLEDGMENTS

These studies were supported by the Deutsche Forschungsgemeinschaft (DFG) in context with the Sonderforschungsbereich 483 “High performance sliding and friction systems based on advanced ceramics.”

REFERENCES

1. K.-H. Zum Gahr and J. Schneider, *Ceram. Int.* **26**:363 (2000).
2. S. Rüdiger, H. Gruhn, R. Heidinger, M. Rohde, J. Schneider, and K.-H. Zum Gahr, *Surface Engineering*, EUROMAT 99-Vol. 11, H. Dimigen, ed. 1999, p. 510.
3. U. Duitsch, S. Schreck, and M. Rohde, *Int. J. Thermophys.* **24**:731 (2003).
4. D. B. Spalding, PH*OENICS Overview, Cham Technical Report: TR 001* (CHAM, United Kingdom, 2001).
5. A. D. Brent and V. R. Voller, *Numerical Heat Transfer* **13**:297 (1998).
6. V. R. Voller and C. Prakash, *Int. J. Heat. Mass Transfer* **30**:1709 (1987).
7. B. Glorieux, F. Millot, and J. C. Rifflet, *Int. J. Thermphys.* **23**:1249 (2002).

8. J. L. Bates, C. E. McNeilly, and J. J. Rasmussen, in *Ceramics in Severe Environments*, W. W. Kriegel and H. Palmour, eds. (Plenum, New York, 1971), pp. 11–25.
9. F. Millot, B. Glorieux, and J. C. Rifflet*, Prog. Astronautics and Aeronautics*. **185**:777 (1999).
10. P. F. Paradis, T. Ishikawa, Y. Saita, and S. Yoda, *Jpn. J. Appl. Phys*. **43**:1496 (2004).
11. Y. S. Touloukian, *Thermophysical Properties of Matter*, Vol. 1 (Plenum, New York, 1970).